
Article:
Surakarnkha, J., Zhaoyuan, L., Gong, P. et al. (4 more authors) (2021) Designing ferrite impregnated epoxy actuators for impact damage detection in carbon fibre reinforced composites. Composites Science and Technology, 216. 109085. ISSN 0266-3538

https://doi.org/10.1016/j.compscitech.2021.109085

Designing ferrite impregnated epoxy actuators for impact damage detection in carbon fibre reinforced composites

[1,2]Jatupol SURAKARNKHA, [1]LEONG Zhaoyuan *, [1]Peng GONG, [1]William HOLMES, [3]Pratik DESAI, [1]Joel FOREMAN, and [1]Nicola MORLEY

[1]Department of Materials Science & Engineering, University of Sheffield, Sheffield, S1 3JD, UK

[2]HMC Polymers Co., Ltd., 20/F, Sathorn City Tower, 175 South Sathorn Road, Thungmahamek, Sathorn, Bangkok 10120, Thailand

[3]Perlemax Limited, Kroto Innovation Centre, 318 Broad Lane, S3 7HQ, Sheffield, UK

*Corresponding author

Abstract

Carbon fibre reinforced polymers composites possess properties that outstrip their component parts, and are seeing increased adoption in sectors such as the aerospace industry. Due to their complex failure mechanisms, it is necessary to have structural health monitoring (SHM) in place. Previous work has shown the efficacy of magnetostrictive materials as damage detection actuators; issues such as their spatial sensitivity require improvement to progress their applicability in SHM. Another requirement is to demonstrate ease-of-fabrication in conjunction to damage detectability, and also to maintain a good weight-to-cost trade-off. In this paper we demonstrate a step-by-step approach to the fabrication and optimisation of an impregnated magnetostrictive epoxy matrix that aims to satisfy these requirements.

Keywords A Polymer-matrix composites (PMCs); A Flexible composites; B Sensing; D Scanning electron microscopy (SEM); Magnetostrictive

1. Introduction

Owing to their exceptional engineering properties, carbon fibre reinforced composites (CFRC) are a class of materials whose use has grown exponentially in past years. This is especially true for

the aerospace industry. High specific modulus and strength compared to conventional metals and alloy systems [1] have led to their adoption in the past several decades, such that the new Boeing 787 is constructed of up to 50% lightweight CFRC. The complex structure of CFRCs, which contributes to their unique properties are also prone to an increased variety of damages such as fibre breakage, debonding, transverse-ply cracking, and delamination [2]. This also means that their failure modes are more complex, hence there are many more routes to potential failure.

The majority of these damages result from low-velocity impact damages, which contribute to material failure during service lifetime. Due to their low-velocity nature, these damages are often difficult to detect and are termed barely visible impact damage (BVID). Incidents that cause them can occur in both in-flight operations and during ground service; *e.g.* dropped tools during servicing, hail storms, avian impacts, and runway debris during take-off. A key problem of BVID is the non-visibility of surface and sub-surface damage leading to the low possibility of accurate visual inspection, whilst the material strength has already been impaired [3]. As a result, composite parts can fail unexpectedly and seriously – combating this is a requirement for turning CFRCs into a robust material for widespread usage within and outside the aerospace industry.

Non-destructive testing (NDT) is the preferred method for investigating BVID (to avoid needless part replacement). Conventional NDT techniques consist of ultrasonic, thermography, radiography, and acoustic emissions techniques [4]. They exhibit reliable results and good sensitivity of detecting damage; however are limited to specialised inspectors, have high time consumption and a high cost of specialised equipment [5].

Magnetostrictive materials experience a change in magnetisation in response to an applied strain [6]. Magnetostrictive materials can be considered for BVID detection [7–10]. Previous studies investigated magnetostrictive wires and ribbons either embedded inside the composite or mounted on the composite surface with specific lay-up patterns. The results exhibited the potential for

damage detection [6,11] and if made into a metamaterial may offer some benefits over conventional NDT. Despite them showing a potential to detect internal strain in the composite reliably, their sensitivity requires improvement so that they are comparable to other strain sensors [6,11]. Another problem in practice is the different lay-up patterns of wires and ribbons can affect the strength of the magnetostrictive response.

One possible alternative is to embed magnetostrictive particles within a suitable flexible matrix [12–17]. Several benefits of fabricating an actuator in this set-up include ease of fabrication for required shapes, ability to tune magnetostrictive response through control of additions, cost effectiveness, and tuneability of mechanical properties [18–20]. A high-sensitivity magnetism/pressure sensor was designed and reported by Xu *et al.* [21] with excellent detection capabilities, which supports this idea.

In the following sections we outline our reasons for selecting the reaction compounds for the fabrication of a novel impregnated epoxy actuator. Following that, we demonstrate the optimisation of the actuator's mechanical properties by modifying the amount of additives, and finally, test the efficacy of the actuator in detecting induced damage from impact tests.

2. Experimental design

2.1. Synthesis route in the design of the actuator matrix

In order to test the efficacy of the proposed actuator design, the system will be tested on prefabricated composite panels using readily available commercial pre-preg. The pre-preg used in this study is the 2 × 2 twill-weave VTC401® from SHD Composite Materials Ltd. Sample fabrication methods will be detailed in the methodology section below.

For high-purity materials iron oxide (ferrite) is less costly than iron, and so was the material of choice to be selected for incorporation into the epoxy matrix. One anticipated issue was that the properties of the actuator had to be adjusted to work with the composite sample that was to be

monitored for damages. A mismatch would lead to either the actuator failing before composite failure (thus negating the whole concept of structural health monitoring), or that the sensitivity of the actuator to any induced strain would be far too low.

Due to this, in addition to the BPA + amine mixture, the decision was made to include a plasticiser to provide improved control over the fabricated actuator's mechanical properties. Flexibilisers can be categorised into 4 types: polyamides, carboxyl-terminated polymers, polyglycol diepoxides, and polysulfides. They introduce higher flexibility, better strain tolerance, and impact strength. In contrast, the disadvantages are a decrease in strength, chemical, and solvent resistance. Hence the flexibiliser:epoxy ratio needs to be carefully selected to optimise for a compromise between both the mechanical properties and resin flexibility.

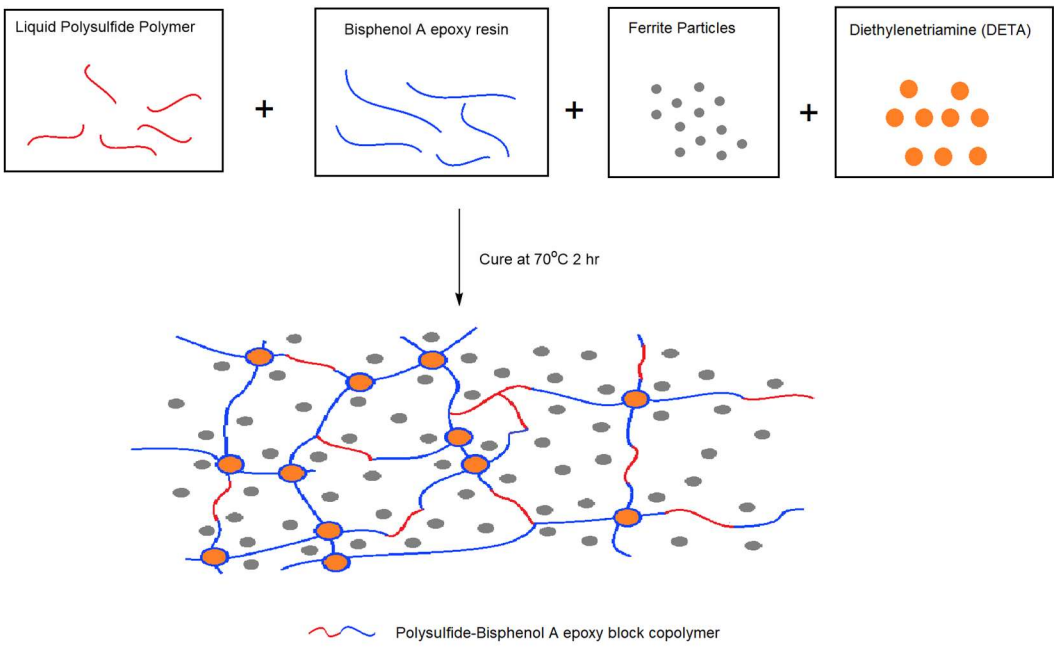

Figure 1. *Proposed components of the new actuator comprising of ferrite particles impregnated into an epoxy matrix in combination with polysulfide additions to tune its elasticity.*

In terms of flexibiliser selection [22], epoxy resin mixed with polygylcol diepoxide showed a high reduction in flexural strength. In the case of carboxyl-terminated polymers such as carboxyl terminated butadiene-acrylonitrile, several unsaturated carbon bonds exist within the structure;

post-fabrication, these double bonds may be exposed to environmental effects (heat, atmosphere, *etc.*) leading to unwanted further curing, resulting in a decrease in flexibility. The system is also susceptible to oxidation reactions, potentially weakening the final synthesised material.

Polysulfide provides wider control of properties over polyamide due its ability to co-cure with either amine or anhydride based catalysts/hardeners. In addition, the utilisation of polysulfide polymer in a ferrite/epoxy system was previously studied and showed no interference with strain sensing [19].. This conclusion supports our argument for the use of the chemical in our system. A Thiokol LP-3, polysulfide polymer, from Wessington Group Ltd. was selected to be used in this work.

The resin chosen as the matrix is a medium-viscosity epoxy resin containing bisphenol A and epichlorohydrin, Epikote 828 purchased from Delta Resins Ltd, while the chosen reaction catalyst is diethylenetriamine (DETA) purchased from Alfa Aesar, and iron oxide (Fe_3O_4) particles were purchased from Goodfellow Cambridge Ltd. The embedded particle sizes are identified through scanning electron microscopy (SEM) and the methodology is discussed below. A truncated process reaction may be given as:

$$\text{Epikote 828} + \text{Amine} + \text{Thiokol Lp3} + Fe_3O_4 \xrightarrow{\Delta} \text{Epoxy} + \text{Ferrite}$$

The components here are shown in Figure 1. The ratio of Epikote 828 to amine may be calculated by utilising its equivalent epoxy weight (EEW) of 184-190g/equivalent – averaged to be 187g/equivalent. Based on this value, the calculated ratio for a stoichiometric reaction is 100:11.

1.2. Design of experiment

As mentioned previously, the ratios of the additions must be carefully considered in order to obtain properties matching that of the VTC401 pre-preg - complementing its elastic modulus of 52.7GPa. The calculated stoichiometric ratio must first be investigated to determine its effect on the mechanical properties of the system (*i.e.* if under-stoichiometry or over-stoichiometry has any deleterious effects on the system). Recipe downselection is two-tiered to reduce experimental

complexity: The first stage only considered the effect of different epoxy:hardener ratios (100:9, 100:11, and 100:13) on the mechanical properties of the cured epoxy sample, which was investigated through 3-point bending tests. The second stage of the experiment was done to optimise actuator properties through varying amounts of ferrite and plasticiser (Thiokol-LP3). A number of samples were fabricated with different amounts of Thiokol LP-3 and ferrite additions to the determined epoxy mixture. All fabricated samples were initially characterised through 3-point bending tests as well as Dynamic Mechanical Analysis (DMA) to correlate their mechanical properties to the glass transition temperature, T_g. Table 1 below shows a full list of the 11 fabricated samples, and their designations, and characterisation tests performed, according to the downselection strategy proposed earlier.

Table 1. *Designation of fabricated samples shown together with their Thiokol LP-3 (T) and ferrite (F) additions. The designations represent Ep: Epoxy, T: Thiokol, and F: ferrite.*

Designation	Thiokol LP-3	Ferrite	3-point bend	DMTA	Strain	Impact test	Magnetisation Mapping
Ep/0T/0F	0	0	Yes	Yes			
Ep/5T/0F	5	0	Yes	Yes			
Ep/10T/0F	10	0	Yes	Yes			
Ep/30T/0F	30	0	Yes	Yes			
Ep/50T/0F	50	0	Yes	Yes			
Ep/5T/10F	5	10	Yes	Yes	Yes	Yes	
Ep/10T/10F	10	10	Yes	Yes	Yes	Yes	
Ep/30T/10F	30	10	Yes	Yes		Yes	
Ep/50T/10F	50	10	Yes	Yes	Yes	Yes	Yes
Ep/5T/20F	5	20	Yes	Yes	Yes		

Ep/10T/20F	10	20	Yes	Yes	Yes

3. Methodology

Composite coupon fabrication. The test CFRC samples were fabricated by laminating 4 plies of VTC-401 twill weave carbon fibre pre-preg, then covering with fluoropolymer releasing film. A breather layer was placed on top to improve the vacuuming process. The layered pre-preg was then bagged and sealed firmly. The bag was checked for air leakage, and then placed into an autoclave and cured at 7 bar and 120˚C for 45 minutes.

Epoxy synthesis. The identification of the epoxy:hardener ratio was prepared by mixing the Epikote 828 resin with different amounts of diethylenetriamine (DETA) hardeners, according to the ratios (100:9, 100:11, and 100:13), which represents understoichiometric, stoichiometric, and overstoichiometric ratios respectively. The mixed epoxy was cured in an oven at 70˚C for 2 hours.

Actuator synthesis. For the fabrication of the other plasticiser-containing and ferrite-containing samples, Epikote 828 was first mixed with Thiokol LP-3, followed by the addition of iron ferrite (Fe_3O_4). The mixture was stirred for at least 3 mins to ensure homogeneity and sonicated at room temperature for 15 mins in an ultrasonic bath (Fisher Scientific, FB 15051) to deagglomerate the iron ferrite particles and improve dispersion. Following this, DETA was added to the mixture to begin the polymerisation process. The mixture was first degassed at room temperature by placing the prepared reagents into a degassing oven at -0.1 MPa for 15 min. Finally, the mixture was poured onto a flat glass plate and cured in an oven at 70˚C for 2 hours.

Synthesis of functionalised composite coupons. The fabrication of functionalised samples was performed by applying the pre-cured actuator mixture onto fabricated VTC401 CFRC coupon samples and following the same curing procedure used to produce the actuators. The thickness of the samples was measured at different points before and after the functionalisation. The thickness

of the applied actuator layer was ground down to 300 micrometers to ensure that the magnetic signal pre-characterisation is kept consistent.

3-point bend. The cured samples were removed from the glass plate post-curing and were cut and polished into various sample sizes. For 3-point bend tests, rectangular samples of 40 x 13 x 1 mm according to ASTM D7264/D7264M – 15 standards were used. From these standards, the rate of crosshead movement or testing speeding can be calculated from as mentioned in ASTM D790-15: $R = \frac{zL^2}{6d}$ where R is crosshead speed (mm/min), z is rate of straining of outer fibre (mm/mm/min) which in this case was imposed to 0.01, L is support span (mm) and d is depth of beam or thickness (mm). 3-point bending testing was set up and conducted in a Zwick/Roell Z050 machine set up in 3-point bending mode, using the built-in extensometer to determine displacement. The extensometer has been previously compared to an optical strain gauge and both values are in agreement. Between three to five repeats for each sample was performed and average values are taken from the data.

DMA tests. The prepared samples were cut and polished into rectangular samples of 30 × 10 × 1.5 mm. The dynamic response of each sample was measured with a Perkin Elmer DMA800 in single cantilever mode by applying a sinusoidal force at 1 Hz. The samples were scanned from room temperature to 200˚C at a heating rate of 3˚C.min^{-1}. The obtained results were obtained in terms of the change in storage modulus, loss modulus and tan(δ) with temperature. Glass transition temperatures (T_g) were determined from the temperature at where the peak of tan(δ) curve occured.

Bending strain test. The sample was cut into rectangular samples of 150 × 50 mm and then placed onto the bending rig which can have four different bending radii; 300, 400, 500, and 600 mm. These can be converted into strain values that are inversely proportional to the bending radii. In order to measure the magnetisation, the HMC5883L AMR magnetic sensor was connected to

the computer. This sensor was chosen as it has been previously characterised against bending strain and compared with inductance readings [/10.1109/INTMAG.2018.8508360]. This sensor was located at the middle of the rig and magnetisation readings before and after bending were recorded through the use of a microcontroller and a computer.

Impact testing. A square sample was initially fabricated to a size of 40 × 40 × 1.4 mm and then placed on the base of the impact equipment. Impact testing was performed by releasing a weighted cone from a specified height through a guidance tube. The impact energy can be calculated from the potential energy of the weighted cone prior to release as: $Impact\ energy = m\ g\ h,$ where *m* is mass (kg), g is gravitational field strength (9.81 $m.s^{-2}$) and *h* is height (m). In this experiment, the weight and height were fixed at 157 g and 1 m, respectively; thus, an impact energy of 1.54 J was employed.

Actuator characterisation. The post-impacted sample surface and actuator surface was first inspected visually and through an Olympus microscope. Further inspection on a field-emission scanning electron microscope (FE-SEM, FEI Inspect F) was performed at a voltage of 10kV. The embedded particles and impact damage were confirmed through microscopy techniques and then imaged. Particle size distribution was determined through Mathematica [23] using the built in functions. The average particle area was determined and from this the particle radius was determined assuming that the particles are spherical.

Magnetic response flaw detection. Magnetisation mapping was used to characterise the magnetisation across the entire sample. Analysis of the results can show the magnetic distribution across the sample graphically through the use of a contour map, from which the effect of damaging specific areas and the associated changes in magnetisation can be investigated. Post-processing was used to interpolate the magnetic readings for the analysis being performed. The sample was subdivided into a grid with 10mm spacings, forming an area of 10 x 10 mm^2. A HMC5883L AMR

magnetic sensor was employed to determine the magnetic field *via* surface contact with the deposited actuator layer. Five repeats on each co-ordinate were determined using the HCM5883L sensor. These results were recorded and post-processed and analysed and presented as a surface plot.

Ultrasonic flaw detection. A transverse ultrasonic probe attached to an Olympus Epoch 600 was used to determine impact damage. A 10mm grid similar to that used for the magnetic response flaw detection was employed; ultrasonic couplant was applied to the probe and it was used to probe the actuator surface along the specified coordinates. The change in time was recorded from the peaks detected and are presented as a surface plot for further analysis.

4. Results and discussion

4.1. Synthesis and characterisation of mechanical properties

The epoxy:hardener stoichiometric ratio was confirmed experimentally (*cf.* Appendix A), taking the amount of ferrite particle and Thiokol additions as the variable experimental parameters. Fabricated samples listed in Table 1 had their mechanical properties characterised through 3-point bend tests, and the obtained flexural strength and modulus results are shown in Figures 2 (a) and (b) respectively.

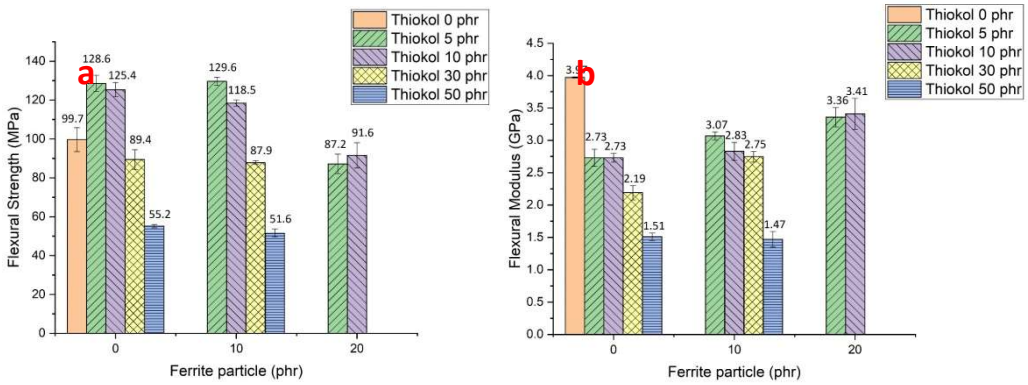

Figure 2. (Left) *Flexural strength; and* ***(Right)*** *Flexural modulus of fabricated samples with different amount of Thiokol additions (0, 5, 10, 30, and 50 phr) and different amounts of ferrite particles (0, 10, and 20 phr). Control: 0 Thiokol, 0 Ferrite phr*

Figure 2 shows the effect on flexural strength of the fabricated samples when ferrite particles as well as when Thiokol were added to the system. From the figure the incorporation of Thiokol plays a central role on flexural strength and modulus of the synthesised system. Increase in Thiokol addition does not always seem to be beneficial; the addition of Thiokol generally increases the flexural strength of the system initially, but beyond a certain percentage, it becomes detrimental. The amount of Thiokol addition that maximises flexural strength appears to vary between 5-10 phr (*per* hundred resin) for each of the 0, 10, and 20 phr Fe additions.

This is attributed to the reaction between Thiokol and epoxy, which forms a polysulfide-epoxy block copolymer. Thiokol, which is a flexible aliphatic chain, (also called a soft domain) reacts with the epoxy, which is a stiff aromatic chain (also called a hard domain). It forms a block copolymer which consists of two parts with two distinct mechanical properties. The stiff domains act as anchors that pins between soft domains, causing physical crosslinking [24–26]. As a result, this crosslinking provides additional strength to the epoxy system. When the addition of Thiokol exceeds a critical value (here observed to be *apx.* >10 phr), the soft domain properties, which possess viscoelastic-like properties, are dominant in the system, leading to a decline in strength.

Another factor affecting mechanical properties is the incorporation of ferrite particles. They possess higher stiffness than the epoxy matrix and behave as a filler to improve the modulus of the system. However, strength is also mitigated as a result. For example, the 10 phr Thiokol sample with no ferrite has a flexure strength of 125.4 MPa, which is 20% higher than the control sample. With the addition of 20 phr ferrite, flexure strength decreases to 91.6 MPa, which is 27% lower than the no ferrite sample and lower than the control sample. This may stem from flaws created by the aggregation of ferrite particles resulting in some stress concentration within material. This kind of stress behaves as weak points that eventually impairs the strength of the system.

DMA is used to determine the glass transition temperature, T_g and results of this characterisation are shown in Figure 3 where T_g decreases with Thiokol addition. For 5 phr Thiokol, the glass temperature is the highest at 119.5 ^{o}C, but drops by 34% for the addition of 50 phr Thiokol. This is attributed to physical crosslinking in the system obtaining from different phases between rubbery and glassy domains. For the lower amount of Thiokol added, this leads to extra crosslinking, which increases the restriction on the polymer chain's rotation/movement, resulting in a higher T_g. Meanwhile, the higher content of Thiokol contributes to the rise of flexible parts in polymer chains leading to a drop in T_g. Comparing the results from the earlier analysis of reactant amounts with the mechanical properties (where the flexural modulus was observed to decrease with increasing Thiokol additions), it can be inferred that a decrease in the glass transition temperature is correlated to this decrease in flexural strength.

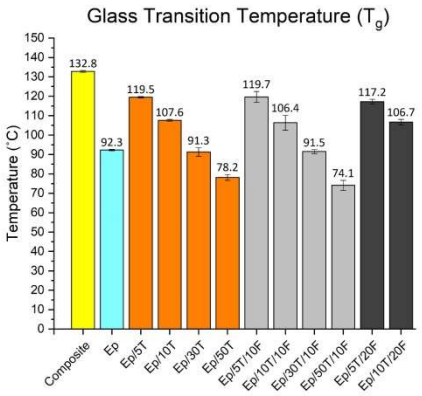

Figure 3. *Experimental results for the DMA characterisation of the fabricated CFRC samples, showing the effect of various additions on the glass transition temperature*

For the incorporation of ferrite particles into the samples, T_g exhibits only a slight difference compared to control samples where no ferrite particles were added. Experimental errors were estimated from the weighting of the sample components. When considering also the standard deviation of these errors, the fluctuations of the results are all observed to fall within the boundaries

of the calculated standard deviations. As a result, it may be concluded that the addition of ferrite particles at this concentration does not influence the T_g of the final material.

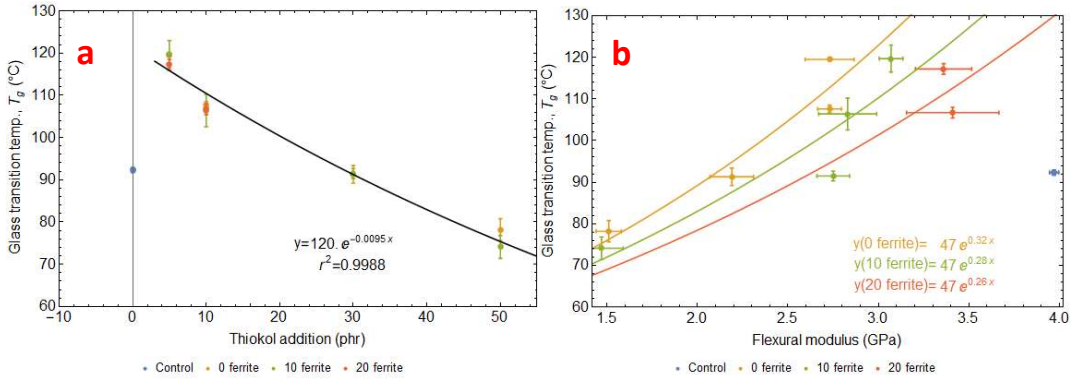

***Figure 4**. **(a)** Change in glass transition temperature as a function of Thiokol addition. The black line is a fit showing the effect of additional addition; **(b)** The effect of the change in glass transition temperature with the flexural modulus.*

Figure 4 shows a numerical fit of the relationships between Thiokol additions and the glass transition temperature. An analytical fit to the data obtained was performed in order to estimate the effect of Thiokol addition on the glass transition temperature for future formulations of the sensor. As expected, addition of Thiokol (which has a glass transition temperature of -50 °C) reduces the glass transition temperature of our mixture. This is true for all samples tested, up to 50 phr. In Figure 4 (right), the glass transition temperature has been plotted against the flexural modulus for the different ferrite additions (0, 10, and 20 in yellow, green, and red). Fitting equations have been used on the data points, and the results show a correlation between the glass transition temperature and the flexural modulus. Generally, Young's modulus is inversely proportional to the ductility of a material. Due to this, for the fabricated actuator layer, it is preferable to select a material that has a lower Young's modulus. Therefore, the main chemical affecting the parameter T_g is Thiokol - 5 phr Thiokol addition is optimal to reach the composite T_g, (apx. 135˚C).

4.2. Expected magnetostrictive behaviour from DLVO theory

During the bending test, the induced strain leads to magnetic reorientation of the particles as more strain is put into the system. In a scenario where only a smaller proportion of the particles have undergone reorientation, the contribution along one axis would be lower in magnitude and sign due to angular effects. The magnetometer setup takes the root square of the magnitudes of the magnetisation detected along the *x*, *y*, and *z* axes respectively, and therefore does not differentiate between the different magnetisation poles (which may be negative). In order to validate this hypothesis an adaptation of the Derjaguin-Landau-Verwey-Overbeek, DLVO theory was employed (by treating the particles in the epoxy matrix as solute/solvent) to determine the effect of particle density distribution on magnetisation. Whilst seemingly a novel approach to this system, the approximations ensure fairly good correlation to experimental evidence. DLVO [27,28] theory can be used to evaluate the free energy between two particles (ferrites) in a solvent (epoxy-thiokol mixture), and has been previously employed for micron-sized particles [29]. The free energy terms consist of the Van der Waals, E_{VdW} and the dual-layer, E_{dl} contributions:

$$E_{DLVO} = E_{VdW} + E_{dl} \tag{1}$$

which can be written as:

$$E_{DLVO} = -\frac{H\,r}{12\,d} + \left(\frac{64\,{k_b}^2\,\varepsilon_0\,\varepsilon_{liquid}\,T^2\,r^2}{q^2\,(d+2\,r)}\right)\left(Tanh(\frac{q\,\varphi(d_p)}{k_b\,T})\right)(e^{-D\,r}) \tag{2}$$

where H is the Hamaker constant, r is the particle size radius, d_p is the distance from the particle, K_b is Boltzmann's constant, ε_0 is the dielectric constant of free space, ε_{liquid} is the liquid's dielectric constant, T is the temperature in Kelvin, q is the elementary charge, and ψ is the potential of the system. The inverse Debye length, D is given as:

$$D = \left(\frac{k_b\,T\,\varepsilon_0\,\varepsilon_{liquid}}{2000\,q^2\,N_A\,EC}\right)^{-0.5} \tag{3}$$

where N_A is Avogadro's number and EC is the electronic charge of the particle. The potential, $\psi(d)$ can be approximated by the sum of the contribution between the hard sphere potential, the dipole-

dipole (solute-solute) interactions, and the magnetic force interaction. Solute-solvent interactions are ignored to simplify calculations.

$$\varphi(d) = E_{HS}(d) + E_{d-d}(d) + E_{MF}(d) \quad (4)$$

A pseudo-Lennard-Jones type hard-sphere potential is used here [30]. Substituting the equations in allows the potential to be rewritten as:

$$\varphi(d) = -\left[50\ E_P \left(\frac{50}{49}\right)^{49} \left[\left(\frac{r}{d}\right)^{50} - \left(\frac{r}{d}\right)^{49}\right] + E_P\right] - \left[\frac{M\ \mu_0}{4\ \pi\ d^3}\right] + \left[\frac{M\ Cos(\theta)}{4\ \pi\ d^2}\right] \quad (5)$$

where E_P is the energy parameter measuring the effective intermolecular attractive strength (typically around 120 K) [30], M is the magnetisation, μ_0 is the permeability of vacuum, and θ is the angle between the field and the internal field of the particle. The constant values (Hamaker, electronic charge, energy parameter, magnetisation) are obtained from similar materials from the literature and are not measured from the sample itself. The objective of these calculations is to provide an overall understanding of how particle sizes and magnetic orientation can affect sensor design, rather than as a numerical study of the energies of the system. The results suggest anisotropy as particle size changes from 1 and 100 μm and as such particle sizes at either end of this range (15 and 100 μm) are used for the study. Furthermore:

1. The DLVO equation is used to determine the positions of any energy minima as a function of the interparticle distance for θ = 0, π/4, 2 π/4, and 3 π/4.
2. The effect of magnetic angle as a function of interparticle distance is computed to determine asymmetric effects

These results are shown in Figure 5 (a) where it is observed that angular asymmetry leads to the presence of a secondary minimum at certain angles which represents colloidal instability. From the energy distribution in Figure 5 (a), the majority of the 15 μm particles will be constrained to interatomic distances of < 5.5 μm which will remain in a colloidal suspension. Figures 5 (a) and (b)

show the difference in energy minimum between 1 and 100 µm particles, suggesting that agglomeration will not be an issue for particles smaller than 15 µm.

The model used here has been simplified to aid the empirical design of ferrite-impregnated epoxy actuators. It is worth mentioning that the theory is based on spherical ferrite powders with the same diameter and spacing in a liquid while ferrite powders in experiments have irregular sizes and unequal spacing in an epoxy.

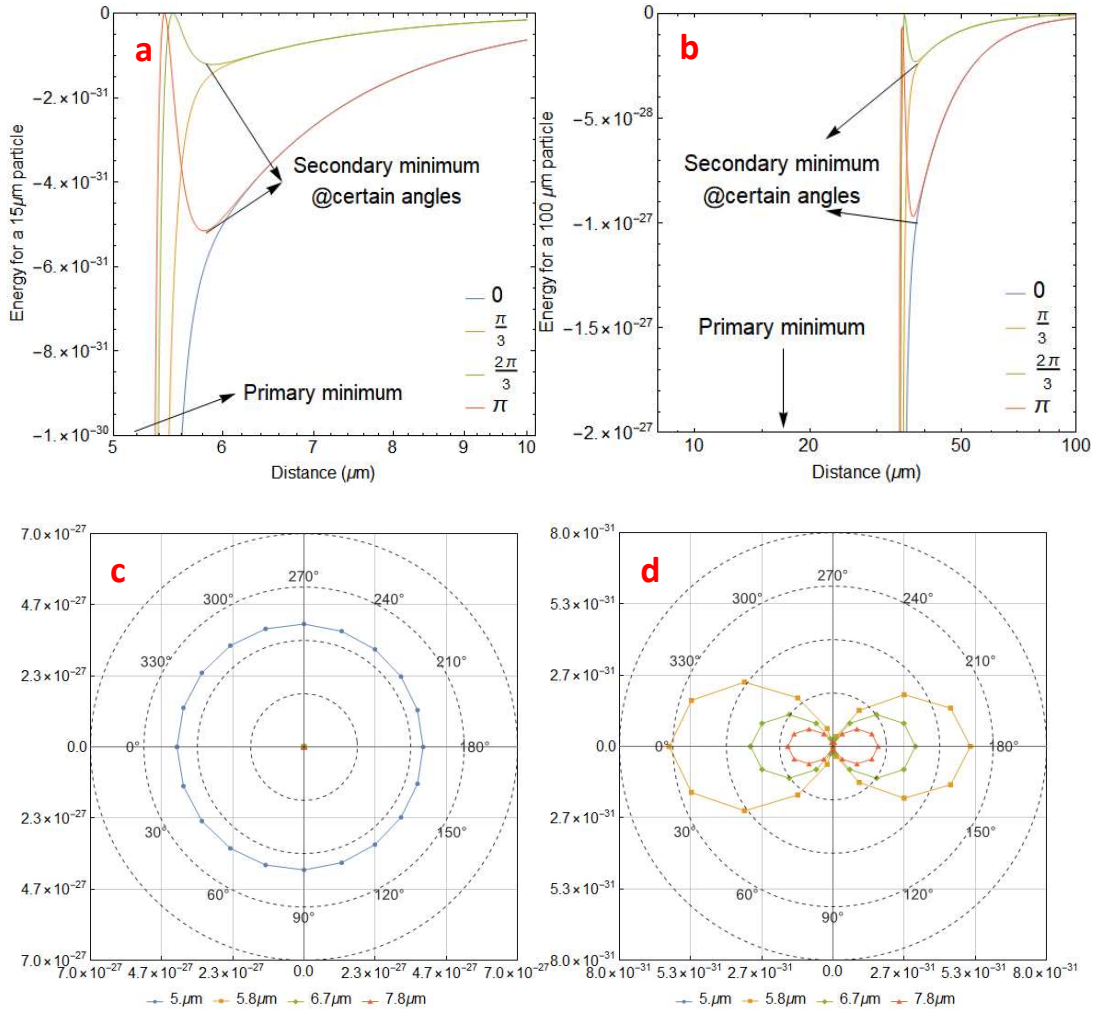

Figure 5 (a) *DLVO energy plot for four angles calculated for a 15 µm magnetite particle,* ***(b)*** *DLVO energy plot for four angles calculated for a 100 µm magnetite particle,* ***(c)*** *Polar coordinate plot of interaction energies of a 15 µm magnetite particle for different interparticle distances 5*

μm, ***(d)*** *Polar coordinate plot of interaction energies of a 15 μm magnetite particle for different interparticle distances 5 – 7.8 μm*

During the curing process of the polymer, the particles are constrained in the epoxy mixture; as the magnetite particles are not field-annealed, magnetic anisotropy will be present in these samples. It is thus more useful to analyse the interaction energies as a function of the interparticle distance. These are shown in Figures 5 (c-d) and show angular anisotropy at larger interparticle distances (>5 μm). Two inferences can be drawn from this data: 1) Because of this anisotropy, for a sample with randomly orientated magnetic domains the particles constrained within the epoxy matrix have different energy barrier levels to be overcome that are dependent on the magnetic domain polarisation. Depending on sensor placement, areas of agglomeration can affect the strain response, leading to unexpected inflections. 2) Because the magnetic particles are constrained by the cured epoxy matrix, they are no longer able to minimise their energies through interparticle distance changes. A secondary pathway for energy reduction may thus occur through magnetic domain angle changes. This will result in non-linear magnetostrictive responses that will have to be included in computer algorithms that seek to use this technology. In order to deal with the issues presented by hypothesis (1), the samples were magnetised in the direction of the shorter y-axis prior to the bending rig tests; bending takes places along the sample's longer x-axis.

The magnetostrictive response of the fabricated samples were tested in a strain bending rig following the procedures outlined in the methods section. The bending radii of 300, 400, 500 and 600 mm can be converted to strain values of 0.33, 0.2, 0.20, and 0.17, respectively. The results from the test are shown in Figure 6a and are plotted against these strain values. From the figure, it can be seen that in general, all samples show an increase in the change of magnetisation from the unstrained samples as a result of increasing strain. The results confirm that the ferrite impregnated epoxy can be used as a magnetostrictive actuator to determine induced strain. A slight inflection

can still be seen for the 0.20 strain results, which may be correlated with the energy barrier required to initially overcome the magnetic angle disorientation. The relationship between the change in magnetisation and the strain is also non-linear; from our analysis we attribute this to the change in magnetic angle due to the constraint of the cured epoxy on the interparticle distance. Physically, this can be attributed to the random orientation of the ferrite powder and thus sensitivity can be improved for further work if the magnetic orientation can be tuned *e.g.* curing the composite in an applied field.

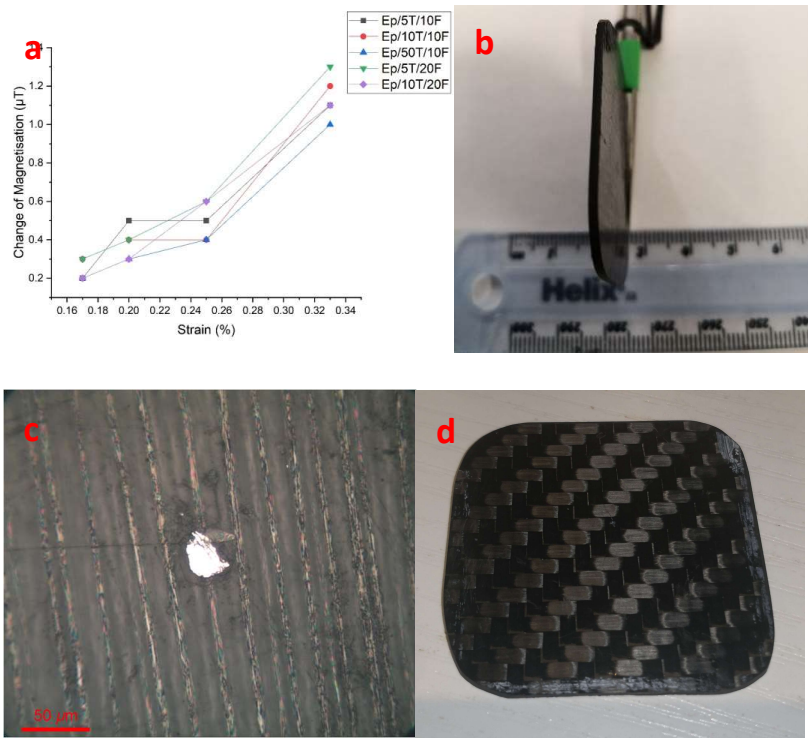

Figure 6. (a) *Relationship between the change in magnetisation obtained from the AMR HMC 5883L sensor and the strain induced into the sample; (**b**) Fabricated VTC401 composite samples with attached actuator layer; a thin epoxy-ferrite actuator was attached to the composite to be used for sensing purposes. The composite+actuator thickness is 1550 μm, while the composite itself is 1220 μm.;* ***(c)*** Optical micrograph of the impact location; and **(d)** Image of the composite sample surface showing no visible damage.

It is observed that there is little difference in the change in magnetisation between the 10 phr and 20 phr samples. This is likely to be due to the dispersion of the ferrite particles in the epoxy and lack of any particle-particle interaction. A lower particle density ensures lesser interference and reduces non-linear response. Thus, due to this marginal difference in magnetostrictive properties between the 10F and 20F samples, we have opted to use the 10F samples as the reduced amount of ferrite addition will lead to a lighter actuator that will help with fuel and cost efficiencies.

4.3. Impact tests on ferrite impregnated epoxy

Based on the above characterisations, we would expect that a lower Young's modulus would be required to function as a sensor. In order to test this, we use the earlier recipes with 10F addition but modifying the amount of Thiokol additions to get different samples with various Young's Modulus values. These samples are: Ep/5T/10F, Ep/10T/10F, Ep/30T/10F, and Ep/50T/10F respectively. We then test these samples via impact tests utilising an impact energy of 1.54 J. This value was chosen as similar impact energies were used in past studies on the efficacy of the VTC401 composites as magnetostrictive actuators, utilising magnetostrictive ribbons as the actuator materials [11]. The impact testing was conducted following the methods outlined earlier.

Our results show that out of all the tested samples, only the Ep/50T/10F survived the impact tests. The other tested samples were found to be too brittle, with samples failing catastrophically on impact tests. For composite samples fabricated from VTC 401 prepreg, the amount of impact energy used was not sufficient to induce catastrophic damage, and as such the samples that did not survive the impact tests are deemed to be unsuitable for further tests. As a result, the Ep/50T/10F recipe was chosen to be coated onto the VTC 401 composite for further tests. These tests were to determine if similar damage detection results could be obtained from the fabricated actuator-composite samples compared to ribbon magnetostrictive actuators in [6,11].

A fabricated VTC 401 composite sample was coated on one side with the Ep/50T/10F ferrite/epoxy mixture as a sensing layer. The sample was cured following the methodology outlined. A prepared sample is shown in Figure 6b. Initial characterisation of this sample was performed utilising a similar HMC 5883L AMR magnetometer setup as used for the previous bending characterisation, and the actuator was polished so that a smooth surface was obtained. Following this, the sample was subjected to impact damage. The actuator coated composite was impact tested with an impact energy of 1.54 J. Figure 6d shows the sample after impact testing, with impact damage not being visible to the eye. Optical microscopy of the sample surface in Figure 6c at the impact site shows damage to the composite surface of approximately 30 µm. Further characterisation was performed using SEM to image the particles in the actuator layer as well as the impact zone.

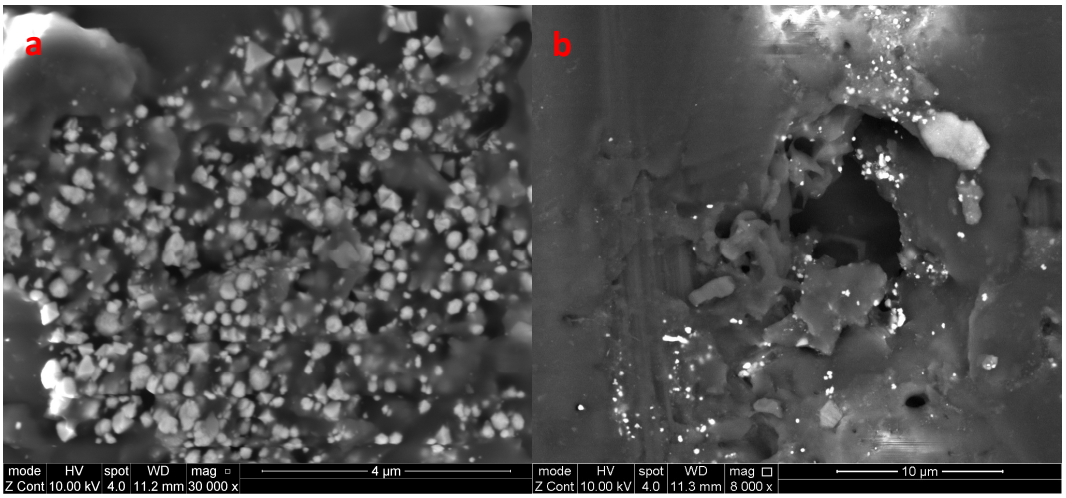

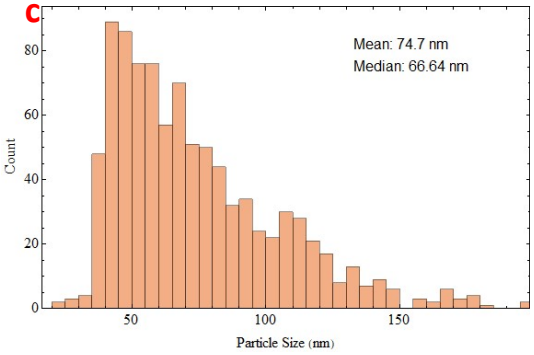

Figure 7. a) SEM micrograph of the actuator layer showing the iron oxide particles in the epoxy matrix; **b)** SEM micrograph of the impact location showing impact damage having penetrated through; **and c)** Histogram of the particle size distribution of the micrograph shown in Figure 7a.

SEM characterisation micrographs are presented in Figure 7 and both the actuator layer on the sample's underside (Figure 7a) and the composite surface (Figure 7b) have been imaged. The particle size distribution was determined from the micrograph with the mean radius as 74.7nm and the median radius as 66.64 nm. Figure 7b shows that the impact damage as penetrated through the sample, and a damage zone of at least 30 μm was observed which is in agreement with the optical micrographs in Figure 6c.

A 10 mm^2 grid for the sample was determined and magnetisation readings were taken for each grid point. At least three repeat readings were made for each coordinate and recorded, and a surface plot was used to visualise the characterisation. The readings from the undamaged sample are used as a reference. This referencing procedure was repeated for each sample to be tested. The change in magnetisation was determined by subtracting these results from the reference results. Figure 8 shows a visualisation of these results as 2D surface plots.

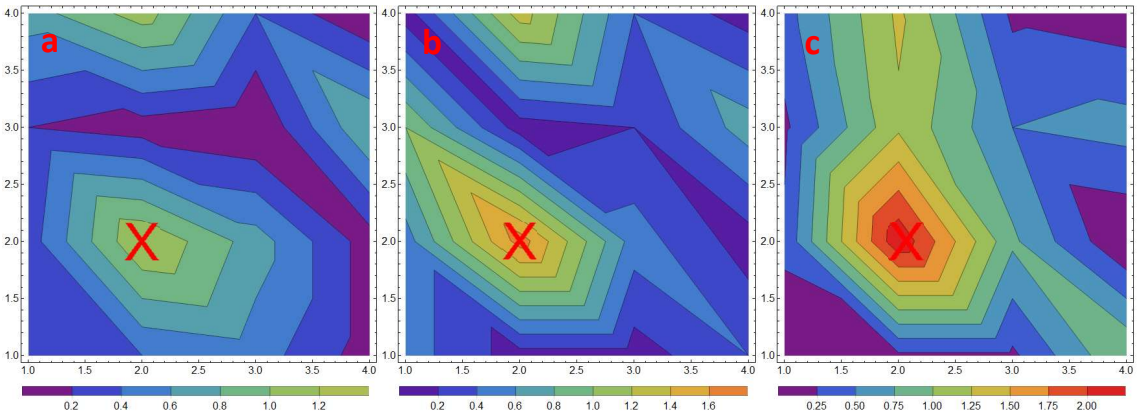

Figure 8. *Change of magnetisation mapping after an impact event of 1.54 J, for* ***(a)*** *1,* ***(b)*** *2 and* ***(c)*** *3 impact events. The red cross marks the impact location. The scale bar at the bottom indicates the change in magnetisation readings in Tesla from the HMC5883L sensor.*

In these samples, the impact location is at the coordinates (2, 2). From Figure 8(a) the impact location exhibits the largest change of magnetisation, which reduces with the distance from the impact point. It may be inferred from these results that the ferrite-impregnated epoxy shows a good indication of its functionality as a sensing actuator.

To further confirm this result, and to verify whether the increasing damage magnitude increases the change in magnetisation, two other impact tests are conducted on the same sample. The additional induced energy is expected to correlate to a proportional increase in detectable damage. Figures 8 (b) and (c) show the changes of magnetisation after performing a second and third impact, respectively.

The maximum recorded magnetisation change for each surface plot is 1.2, 1.7, and 2.2 μT for the first, second, and third consecutive impacts respectively. The results reveal that the accruing increased impact damage at the same location significantly influences the magnitude of the magnetisation change that is being recorded. This validates the functionality of the fabricated actuator. The largest change comes from the initial impact, (1.2 μT); and this may be attributed to a combination of the magnetostrictive properties of the samples as well as contributions from flux leakage. This inference is in agreement by previous work which has demonstrated the possibility of VTC 401 composites failing when impact damage of 1.63 J was induced on a 12 × 5 cm^2 sample. The impacted sample was then characterised utilising ultrasonic flaw detection on a similar sparse grid that was used for the magnetostrictive characterisation. The results are shown as a surface plot in Figure 9(b), showing good agreement with the detection determined utilising the AMR HMC 5883L sensor (shown again in Figure 9(a) for comparison). Further analysis was

performed by considering the magnitude of the readings away from the impact site coordinates (2, 2) for both tests, and these results are shown in Figure 9(c). The magnetostrictive dataset was fitted with an equation to approximate the magnetostrictive behaviour of the actuator:

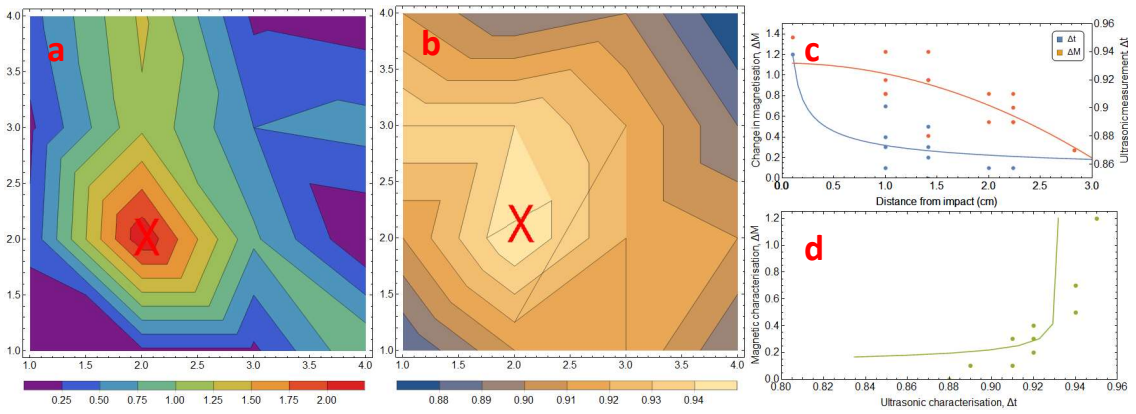

Figure 9. *Comparison of magnetostrictive ferrite-epoxy actuators for a damage-impacted samples through* ***(a)*** *Magnetostrictive characterisation (values are in ΔM (μT)), and* ***(b)*** *Ultrasonic characterisation for these samples. The red crosses mark the impact location.* ***(c)*** *Change in magnetisation and ultrasonic characterisation as a function of distance from the impact point,* ***(d)*** *Shows the change in magnetisation as a function of ultrasonic characterisation. The solid lines are a fit to the data to illustrate the trends.*

$$y = \frac{a}{x^2} + b\sqrt{c/x} \tag{6}$$

where the x^{-2} term of the equation represents the magnetisation decay away from the impact location, and the $x^{-1/2}$ term represents the effect of the stress propagation through the composite as a function of the impact, using a generalised Griffith equation. The ultrasonic results are fitted to a square term to approximate the volume expansion of the composite from the impact site. Both datasets are plotted against each other in Figure 9(d), together with their fitting equations. The dataset, in agreement with the surface plots, show a good corelation with one another.

4.4. Comparison with magnetostrictive ribbons as actuators

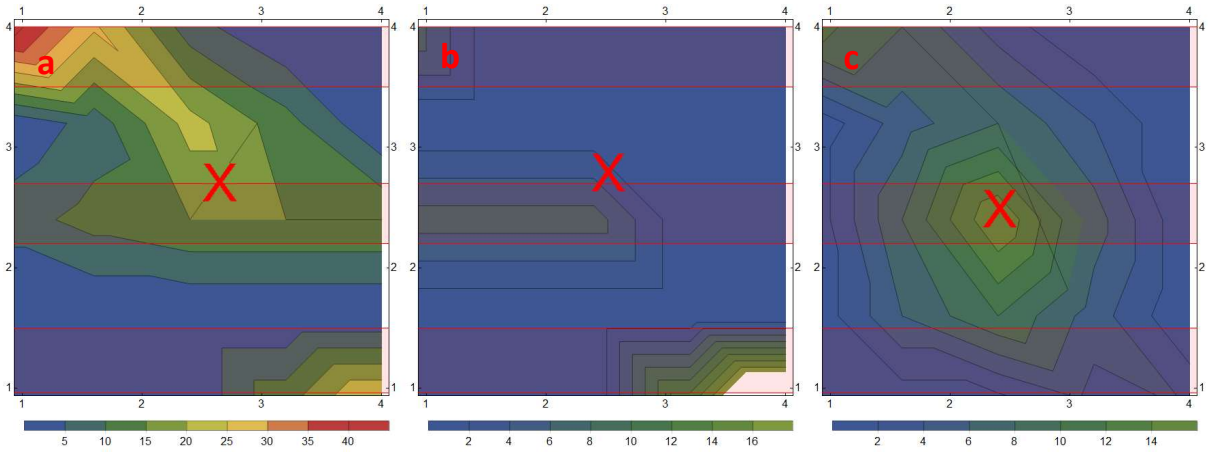

Figure 10. *VTC 401 composite samples* ***(a)***, ***(b)***, *and* ***(c)*** *fabricated utilising magnetostrictive ribbons as composite actuators. The red crosses mark the impact location, while the red-shaded regions indicate the positions of the amorphous CoSiB magnetrictive ribbons.*

As a final check to compare the efficacy of magnetostrictive ferrite-impregnated-epoxy as strain actuators, we fabricate a similar sized sample utilising instead of the ferrite-impregnated-epoxy, amorphous CoSiB magnetostrictive ribbons as actuators. Characterisation again used the AMR HMC 5883L sensor and an impact energy of 1.54 J, with the fabrication details outlined further in the methods section. From Figure 10, the magnetostrictive ribbons with the AMR sensor were sensitive to the position of the impact damage. The change in magnetisation was found to be strongly dependant on the impact location – whether the impact was over the magnetostrictive ribbon (thus straining the ribbon directly if mounted topside), or if it missed the ribbon, contributing a reduced strain field. From Figures 10(a) and (b), large magnetisation readings detected coincide with the positioning of the magnetostrictive ribbons, and only a direct impact produced a surface map that is comparable to the epoxy-ferrite actuator. This is due to the large magnetisation of the CoSiB ribbon (*apx.* 20 μT), measured using a Hall-effect probe), in comparison to the impact energy's smaller change in magnetisation. We note that co-cured ribbons can therefore introduce additional signal and noise to the composite samples and an

epoxy coating layer on the sample can serve to reduce this noise and confer better accuracy as an actuator.

5. Conclusions

In conclusion, we have hypothesised that the fabrication of ferrite impregnated epoxy can function as a replacement for composite surface mounted magnetostrictive ribbons as damage actuators. In order to test the hypothesis, we have designed an experiment to select an appropriate recipe for the actuator and have found that:

- Thiokol additions can be used to tune the ductility of the actuator so that a good match between the mechanical properties composite and the actuator can be achieved. This helps to ensure that the actuator does not fail before the composite.
- Increased ferrite additions to the system does not change the magnetostrictive sensitivity, likely because the ferrite particles do not exhibit strong ferromagnetic behaviour. Better magnetostrictive materials are required to optimise actuator behaviour and sensitivity
- Despite the low sensitivity of the ferrite particles, damage induced *via* impact testing is shown to be detectable. A contour map of the results shows clearly the region of impact damage, and its effect on subsequent impacts.
- When compared to surface mounted ribbons as actuators, the use of the ferrite impregnated epoxy showed more consistent results.

Acknowledgements: This work was in part funded under the Cleansky2 scheme, for the project SHERLOC JTI-CS-2009-01-GRA-01-005. The authors would also like to thank J. Leach and R. Ramsdale-Capper for their help during the fabrication process.

Contribution breakdown: Writing: JS (35%), ZL (40%), PG (5%); NAM (20%); Experimental: JS (70%), ZL (10%), PG(10%); WH (10%); DOE: ZL (65%), NAM (20%), JS (15%); Figures: JS (55%), ZL (45%); Analysis: JS (20%), ZL (40%), NAM (10%), PD (30%).

References

[1] V. Giurgiutiu, Structural health monitoring of aerospace composites, 2016. http://www.sciencedirect.com/science/book/9780124096059 (accessed March 5, 2019).

[2] W.J. Cantwell, J. Morton, Detection of impact damage in CFRP laminates, Composite Structures. 3 (1985) 241–257. https://doi.org/10.1016/0263-8223(85)90056-X.

[3] X.C. Sun, S.R. Hallett, Barely visible impact damage in scaled composite laminates: Experiments and numerical simulations, International Journal of Impact Engineering. 109 (2017) 178–195. https://doi.org/10.1016/j.ijimpeng.2017.06.008.

[4] S. Gholizadeh, A review of non-destructive testing methods of composite materials, Procedia Structural Integrity. 1 (2016) 50–57. https://doi.org/10.1016/j.prostr.2016.02.008.

[5] K. Diamanti, C. Soutis, Structural health monitoring techniques for aircraft composite structures, Progress in Aerospace Sciences. 46 (2010) 342–352. https://doi.org/10.1016/j.paerosci.2010.05.001.

[6] A. Al-Taher, R.W. Reiss, A.D. Lafferty, S.A. Hayes, N. Lupu, I. Murgulescu, N.A. Morley, Magnetostrictive Materials for aerospace applications, Journal of Physics: Conference Series. 903 (2017) 012010. https://doi.org/10.1088/1742-6596/903/1/012010.

[7] A.G. Olabi, A. Grunwald, Design and application of magnetostrictive materials, Materials & Design. 29 (2008) 469–483. https://doi.org/10.1016/j.matdes.2006.12.016.

[8] Z. Leong, W. Holmes, J. Clarke, A. Padki, S. Hayes, N.A. Morley, Magnetostrictive Sensors for Composite Damage Detection and Wireless Structural Health Monitoring, IEEE Trans. Magn. 55 (2019) 1–6. https://doi.org/10.1109/TMAG.2019.2899537.

[9] Q.A. Abbas, N.A. Morley, Fabrication and characterization of magnetostrictive amorphous FeGaSiB thin films, Journal of Magnetism and Magnetic Materials. 439 (2017) 353–357. https://doi.org/10.1016/j.jmmm.2017.04.097.

[10] D. Seifu, A.J. Hall, D. Elbert, P. McGuiggan, O.J. Myers, R.C. Budhani, Magnetostrictive particulates of $Tb_{0.3}Dy_{0.7}Fe_2$ integrated into carbon fiber reinforced polymer for structural damage monitoring, AIP Advances. 10 (2020) 075204. https://doi.org/10.1063/5.0013282.

[11] Z. Leung, A. Al-Taher, L. Chan, N. Walters, M. McGahan, S. Hayes, N. Lupu, I. Murgulescu, N. Morley, Structural Health Monitoring using magnetostrictive sensors, in: 2017 IEEE International Magnetics Conference (INTERMAG), IEEE, Dublin, Ireland, 2017: pp. 1–1. https://doi.org/10.1109/INTMAG.2017.8007893.

[12] J.D. Lopez, A. Dante, C.C. Carvalho, R.C.S.B. Allil, M.M. Werneck, Simulation and experimental study of FBG-based magnetic field sensors with Terfenol-D composites in different geometric shapes, Measurement. 172 (2021) 108893. https://doi.org/10.1016/j.measurement.2020.108893.

[13] B. Li, T. Zhang, C. Jiang, J. Gu, Low eddy current loss of Terfenol-D/epoxy particulate magnetostrictive composites prepared using the particle phosphatizing treatment method, Journal of Magnetism and Magnetic Materials. 508 (2020) 166869. https://doi.org/10.1016/j.jmmm.2020.166869.

[14] J.D. Lopez, A. Dante, A.O. Cremonezi, R.M. Bacurau, C.C. Carvalho, R.C. da Silva Barros Allil, E.C. Ferreira, M.M. Werneck, Fiber-Optic Current Sensor Based on FBG and Terfenol-D With Magnetic Flux Concentration for Enhanced Sensitivity and Linearity, IEEE Sensors J. 20 (2020) 3572–3578. https://doi.org/10.1109/JSEN.2019.2959231.

[15] Z. Wang, K. Mori, K. Nakajima, F. Narita, Fabrication, Modeling and Characterization of Magnetostrictive Short Fiber Composites, Materials. 13 (2020) 1494. https://doi.org/10.3390/ma13071494.

[16] X. Lv, J. Liu, Q. Ding, M. Wang, Z. Pan, Textured Orientation and Dynamic Magnetoelastic Properties of Epoxy-Based TbxDy0.7–xPr0.3(Fe0.9B0.1)1.93 Particulate Composites, J Supercond Nov Magn. 33 (2020) 3857–3864. https://doi.org/10.1007/s10948-020-05648-2.
[17] B. Li, T. Zhang, Y. Wu, C. Jiang, High-performance magnetostrictive composites with large particles volume fraction, Journal of Alloys and Compounds. 805 (2019) 1266–1270. https://doi.org/10.1016/j.jallcom.2019.07.164.
[18] R. Elhajjar, C.-T. Law, A. Pegoretti, Magnetostrictive polymer composites: Recent advances in materials, structures and properties, Progress in Materials Science. 97 (2018) 204–229. https://doi.org/10.1016/j.pmatsci.2018.02.005.
[19] S.H. Lim, S.R. Kim, S.Y. Kang, J.K. Park, J.T. Nam, D. Son, Magnetostrictive properties of polymer-bonded Terfenol-D composites, Journal of Magnetism and Magnetic Materials. 191 (1999) 113–121. https://doi.org/10.1016/S0304-8853(98)00315-1.
[20] C. Rodríguez, M. Rodriguez, I. Orue, J.L. Vilas, J.M. Barandiarán, M.L.F. Gubieda, L.M. Leon, New elastomer–Terfenol-D magnetostrictive composites, Sensors and Actuators A: Physical. 149 (2009) 251–254. https://doi.org/10.1016/j.sna.2008.11.026.
[21] J. Xu, L. Pei, J. Li, H. Pang, Z. Li, B. Li, S. Xuan, X. Gong, Flexible, self-powered, magnetism/pressure dual-mode sensor based on magnetorheological plastomer, Composites Science and Technology. 183 (2019) 107820. https://doi.org/10.1016/j.compscitech.2019.107820.
[22] A. Christopoulos, E. Hristoforou, G. Tsamasphyros, Strain sensing capabilities of iron/epoxy composites, Smart Materials and Structures. 21 (2012) 085030. https://doi.org/10.1088/0964-1726/21/8/085030.
[23] W. Research, Mathematica 10.4, 10.4, Champaign, Illinios, 2016.
[24] R.A. Shanks, I. Kong, General Purpose Elastomers: Structure, Chemistry, Physics and Performance, in: P.M. Visakh, S. Thomas, A.K. Chandra, Aji.P. Mathew (Eds.), Advances in Elastomers I, Springer Berlin Heidelberg, Berlin, Heidelberg, 2013: pp. 11–45. https://doi.org/10.1007/978-3-642-20925-3_2.
[25] G.Z. Zhang, Z.K. Fan, Y.W. Quan, Q.M. Chen, The preparation and physical properties of polysulfide-based elastomers through one-pot thiol-ene click reaction, Express Polymer Letters. 7 (2013) 577–584. https://doi.org/10.3144/expresspolymlett.2013.55.
[26] M. Abdouss, T. Farajpour, M. Derakhshani, Investigating of polysulfide and epoxy-polysulfide copolymer curing. Untersuchungen zur Copolymer-Aushärtung von Polysulfiden und Epoxy-Polysulfiden, Materialwissenschaft Und Werkstofftechnik. 41 (2010) 884–888. https://doi.org/10.1002/mawe.201000680.
[27] E.J.W. Verwey, Theory of the Stability of Lyophobic Colloids., J. Phys. Chem. 51 (1947) 631–636. https://doi.org/10.1021/j150453a001.
[28] B. Derjaguin, L. Landau, Theory of the stability of strongly charged lyophobic sols and of the adhesion of strongly charged particles in solutions of electrolytes, Progress in Surface Science. 43 (1993) 30–59. https://doi.org/10.1016/0079-6816(93)90013-L.
[29] M. Zhang, Q. Liu, J. Liu, Extended DLVO theory applied to coal slime-water suspensions, J. Cent. South Univ. 19 (2012) 3558–3563. https://doi.org/10.1007/s11771-012-1443-1.
[30] J. Jover, A.J. Haslam, A. Galindo, G. Jackson, E.A. Müller, Pseudo hard-sphere potential for use in continuous molecular-dynamics simulation of spherical and chain molecules, The Journal of Chemical Physics. 137 (2012) 144505. https://doi.org/10.1063/1.4754275.